Materials Research. 2024; 27:e20240022
DOI: https://doi.org/10.1590/1980-5373-MR-2024-0022

Microstructure and Mechanical Properties of Laser Welded Joint of Cerium-Containing Magnesium Alloy

***Jin Yin*[a,*], *Zhiyu Chen*[b], *Xiajuan Dai*[a], *Zhuyang Chen*[a], *Yuan Cui*[a]**

[a]*Jiangsu University of Technology, School of Electrical & Information Engineering, 213001, Changzhou, Jiangsu, PR China.*
[b]*Taiyuan University of Technology, College of mechanical and vehicle engineering, 030024, Taiyuan, Shanxi, PR China.*

Received: January 17, 2024; Revised: April 01, 2024; Accepted: April 28, 2024

The modification of magnesium alloy through the addition of rare-earth elements improves specific properties of magnesium alloy. However, the evolution mechanisms of rare-earth precipitates during thermal cycles are still unclear, particularly during the welding thermal cycles. Therefore, deep research on the influence mechanisms of rare-earth precipitates on the welded joint is necessary. In this paper, Ce-containing Mg alloy was successfully welded by laser welding. The microstructure of the welded joint was deeply analyzed. As a result, the elemental composition and distribution rules of precipitates within the fusion zone were obtained. In addition, heat treatment was carried out for the welded joint, thus deducing the evolution mechanisms of precipitates within the joint. The corresponding results revealed that typical micron/sub-micron-sized particles, consisting of both conventional and rare-earth intermetallics, are formed and neatly distributed within the fusion zone, demonstrating that the rare-earth particles inside the fusion zone are much smaller in size than that of $Mg_{17}Al_{12}$. Tensile test results suggest that these tiny particles significantly improved the strength of the fusion zone, promoting the tensile-shear strength of the joint accounting for 76.6% of that of the base metal. The above approach provides a feasible solution for the welding of rare-earth Mg alloys.

Keywords: *Rare-earth magnesium alloy, Laser welding, Microstructure, Mechanical properties, Cerium.*

1. Introduction

The energy crisis and increasing environmental pollution force the industrial production field to put forward higher requirements for lightweight materials[1]. Magnesium (Mg) alloys, as the most potentially lightweight metallic materials, are widely used in automotive, aviation/aerospace, railway transit, and other areas that need reducing weight and energy consumption[2-5]. However, due to the hexagonal close-packed (HCP) crystal structure and unique (Mg)$1s^2 2s^2 2p^6 3s^2$ outer electronic structure of the Mg atom, pure magnesium is inherently a material with low strength and plasticity[6], which seriously limits the application of magnesium alloys in engineering applications.

To improve the strength and ductility of Mg alloys, alloying elements are elaborately added, promoting the formation of strengthening precipitates within the alloys. In recent years, the compositional improvement of traditional magnesium alloys has attracted more attention[7]. Rare-earth elements, due to their unique physical and chemical properties[8], produce various strengthening mechanisms such as solid solution strengthening, grain refinement strengthening, precipitation strengthening, and aging strengthening within magnesium alloys, exhibiting their unique advantages in improving the performance of magnesium alloys.

Cerium (Ce) is a light rare-earth element commonly used to optimize the composition of magnesium alloys. The effect of Ce on the microstructure and properties of magnesium alloys has been partially studied[9-12]. For instance, Li et al.[13] reported that the addition of Ce to AZ31 magnesium alloy triggered the formation of a new phase, Al_4Ce, in the alloy, inhibiting the formation of β-$Mg_{17}Al_{12}$ in the alloy and refining the grains. When the content of Ce in the alloy reaches 4%, the grains obtain their minimal size. Li et al.[14] further studied the effect of Ce on the hot deformation behavior and microstructure evolution of magnesium alloys. The results showed that the rare-earth intermetallics formed from Ce lead to the pinning of dislocations and grain boundaries, hindering the dislocation movement and grain boundary migration, resulting in the ultimate tensile strength improvement of the alloy. Furthermore, the Al_4Ce particles elevate the driving force of recrystallization, promoting dynamic recrystallization and reducing the dislocation density. Juan et al.[15] also reported a similar effect of rare-earth Ce on the alloying of the as-cast AZ (Mg-Al-Zn) system.

It is worth noting that most of the precipitates within Mg alloys possess poor thermal stability. Therefore, in-depth research on the evolution mechanisms of these precipitates, including precipitates consisting of both conventional elements and rare-earth elements, during the thermal cycles is crucially important. It is well-acknowledged that laser welding is a fusion welding process that contains typical thermal cycles[16]. Interestingly, precipitates within the fusion zone may melt and homo-dispersed during the laser welding operation under

*e-mail: yinjin2023@gmail.com

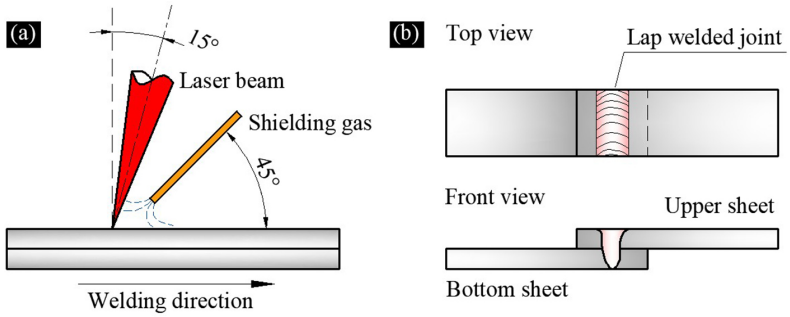

Figure 1. Schematic diagram of laser welding. (a) Laser welding, (b) lap welded joint.

Table 1. The chemical composition of the base metal (wt. %).

Element	Al	Zn	Ce	Mn	Si	Fe	Mg
Content	3.156	1.098	0.4	0.385	0.167	0.029	Bal.

the stirring effect of the laser beam. Consequently, welded joints, with characteristics like enhanced fusion zone, narrow heat-affected zone, and deep weld penetration are obtained[17]. Therefore, the combination of laser welding and rare-earth precipitates possesses great potential in achieving high-quality welding of Mg alloys. However, it is noteworthy that the corresponding mechanisms regarding these enhancements are still unclear, particularly when rare-earth precipitates are involved. Evidently, in-depth research is needed.

In this paper, laser welding is employed, and Ce-containing AZ31 magnesium alloy is successfully welded. With the help of a variety of characterization methods, the microstructure of the welded joint is analyzed in detail, revealing that micron/sub-micron-sized particles are formed and neatly distributed within the fusion zone. Substantially, solution treatment is carried out. As a result, the phase composition of the micron/sub-micron-sized particles is evaluated, and the distribution rules and evolution mechanisms of particles consisting of both conventional elements and rare-earth elements are obtained. Utilizing tensile-shear tests and fracture observation, the contribution of these tiny particles to the strength improvement of the welded joint is deduced. The above results provide a feasible solution for improving the welding quality of rare-earth Mg alloys.

2. Experiment Details

2.1. Materials used

The material used in this work is a rare-earth Mg alloy, specifically an AZ31 as-cast magnesium alloy containing 0.4 wt.% Ce. The rare-earth Mg alloy ingot was cut into sheets with sizes of 40×20×0.7 mm. The chemical composition and mechanical properties of the base metal are shown in Table 1 and Table 2. Prior to welding, the surface of the sheets was polished with 1000# abrasive sandpaper, then the sheets were completely cleaned and dried before correctly attaching to the welding table.

2.2. Welding parameters

The laser welding equipment used in this work is an IPG YLS-2000TR fiber laser, integrating within a KUKA KR 30 R2100 robotic arm. The welding form was lap-weld, and the lap distance was 20 mm. During the welding operation, the end face of the laser head is 47 mm away from the upper surface of the workpiece, facilitating a defocusing distance (Δf) of 0 mm and a laser beam of 0.3 mm in diameter on the upper surface of the workpiece. It is worth noting that the laser beam is tilted 15° from the vertical direction, forming a 75° angle with the welding direction. Shielding gas during welding operation is pure argon. The blowing direction is 45° from the welding direction, and the flow rate is 20 L/min. The protective atmosphere continues consistently until the welded joint is completely cooled. Welding parameters were set as follows: a welding power (P) of 500 W, and a welding speed (V) of 80 mm/s. The schematic diagram of laser welding is described in Figure 1, and the welding parameters are listed in Table 3.

Table 2. The mechanical properties of the base metal.

Materials	Ultimate Tensile strength	Elongation
AZ31-0.4%Ce	180 MPa	13%

Table 3. Welding parameters.

P (W)	V (mm/s)	Δf (mm)
500	80	0

2.3. Test details

In order to investigate the microstructure of the welded joint, metallographic samples were prepared in advance. The test samples were cut perpendicularly to the center of the welded joint with the help of a linear cutting machine, followed by inlaying, grinding, polishing, and etching. The etching agent was prepared with 1 ml nitric acid, 1 g oxalic acid, and 98 ml water, and the etching time was 10 s. The microstructure of the welded joint was observed by Zeiss Axioscope A1 optical microscope (OM) and Zeiss EVO MA 10 scanning electron microscope (SEM). The elemental composition of the intermetallics within the welded joint was examined with the Oxford X-Max energy dispersive

spectrometer (EDS) integrated with Zeiss SEM. A tensile test was carried out at a Care IBTC-5000 in-suit tensile system with a stretching speed of 1mm/min. Thereafter, the fracture of the sample was observed through SEM, thus analyzing the fracture mechanism of the welded joint.

3. Results and Discussion

3.1. Microstructural observation of joint

The cross-sectional morphology of the welded joint is shown in Figure 2. Evidently, the upper and bottom sheets are effectively connected. Obvious defects, such as microcracks and micropores, are rarely observed in the cross-sectional morphology. Interestingly, the weld is slightly raised and the fusion zone is funnel-shaped, with the width of the fusion zone at the top surface of the welded joint being 1087 μm, while that at the contact interface of two sheets being 810 μm, both are wider than the thickness of a single sheet, indicating the robust connection of the two sheets.

Back-scattered electron (BSE) images in Figure 3(b) and Figure 4(a) indicate that precipitates in base metal are needle-like and island-shaped, with the length of needle-like precipitates being approximately 20 ~ 40 μm, and the width and length of island-shaped precipitates being approximately 20 × 50 μm. The metallographic images of precipitates in the base metal displayed in Figure 3 highly support the above observations, and the XRD spectrums in Figure 3(c) indicate that the phase composition of these precipitates is mainly $Mg_{17}Al_{12}$, $Al_{11}Ce_3$, and $Al_{10}Ce_2Mn_7$. It is worth noting that large-sized precipitates originally in base metal are not observed within the fusion zone, and tiny particles are found instead, as depicted in Figure 2(b). Moreover, obvious heat-affected zones located beside the fusion zone are also not observed. Clearly, further analysis is needed to clarify the microstructure of the fusion zone and heat-affected zone.

3.2 Microstructure and composition of the fusion zone

A magnified view of the fusion zone through an optical microscope found an interesting phenomenon, namely precipitates in the fusion zone are almost transformed completely into tiny particles. The metallographic images in Figures 4(c-d) indicates that the diameters of these particles are lower than 1 μm, suggesting that the laser beam and the corresponding melting of the fusion zone promote the refinement of large-sized precipitates originally in the base metal. Interestingly, sporadic needle-like precipitates can still be found in the fusion zone, and their color in OM is close to that of the tiny particles, indicating their similar phase composition. However, residual island-shaped precipitates can not be found in the fusion zone, which is closely related to the melting points and evolution mechanisms of precipitates originally in the base metal during thermal cycles.

SEM observations of the fusion zone are detailed in Figure 5, which are consistent with the results found in

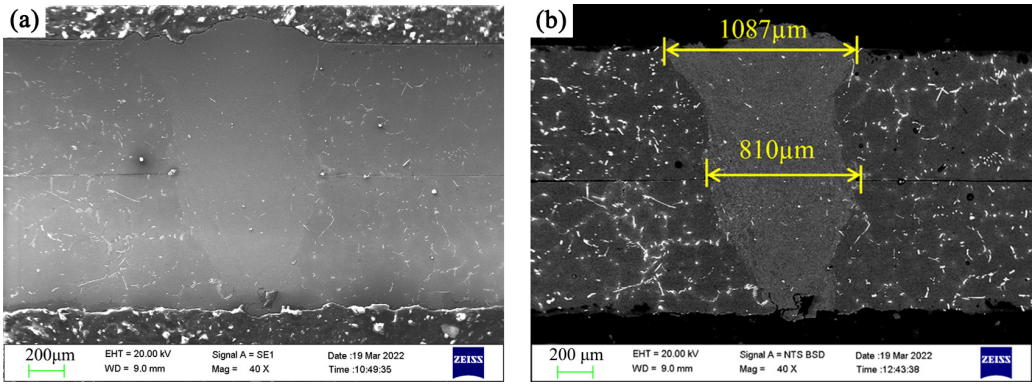

Figure 2. Sectional morphology of the welded joint. (a) SEM image, (b) BSE image.

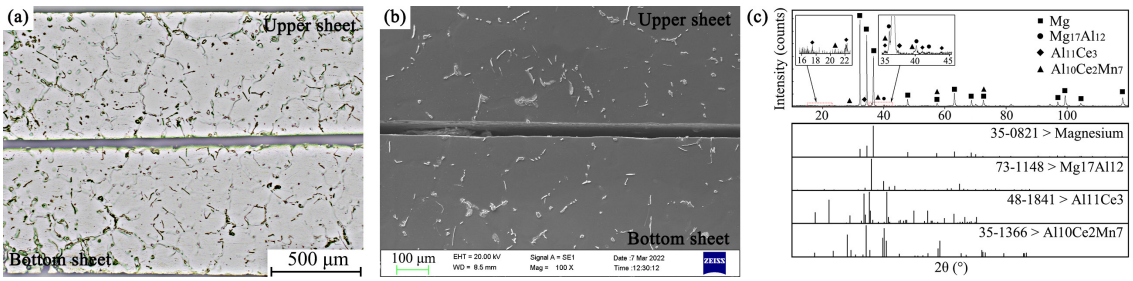

Figure 3. Microstructure and XRD analysis of the base metal. (a) OM image of the base metal, (b) SEM image of the image, (c) XRD results of the base metal.

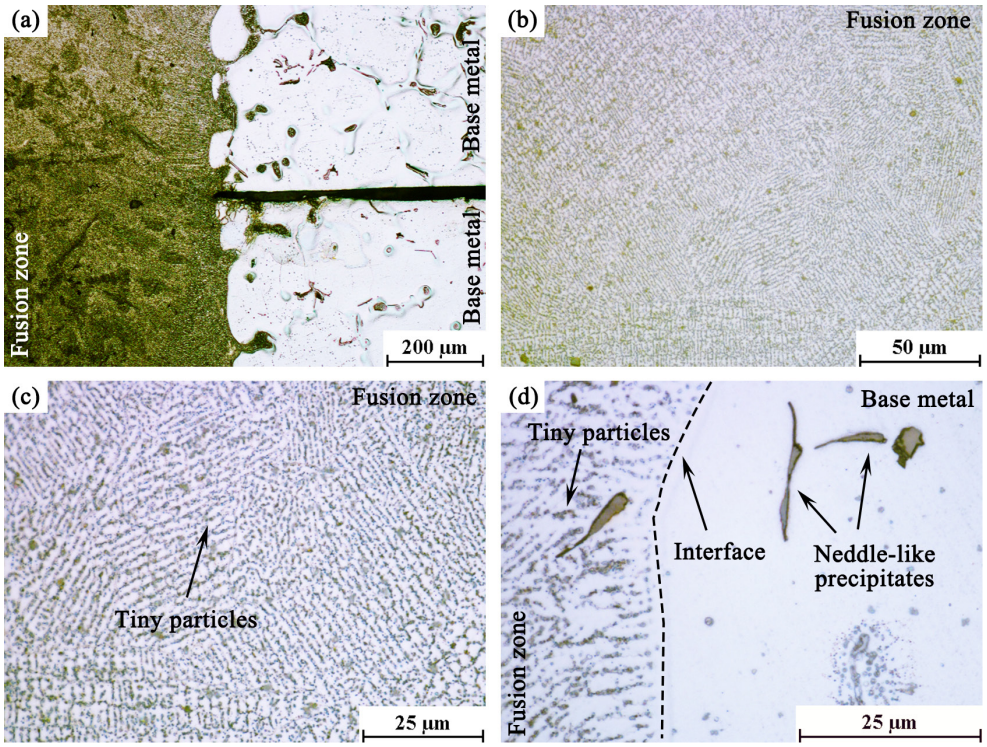

Figure 4. OM images of the fusion zone. (a) the interface of the fusion zone, (b) the fusion zone, (c) the magnified view of the fusion zone, (d) the magnified view of the interface.

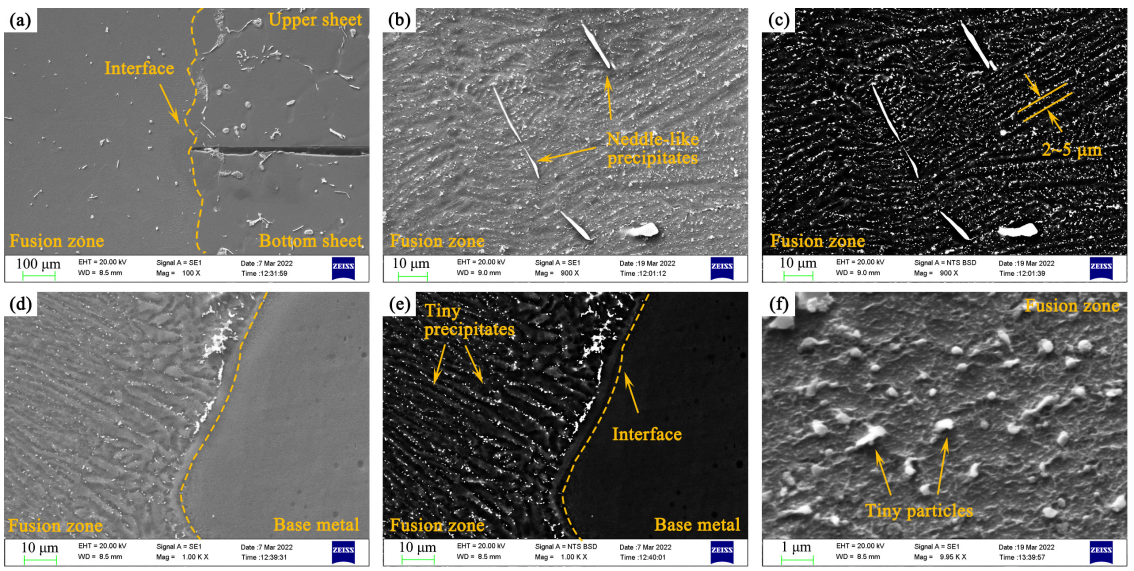

Figure 5. SEM image of the fusion zone. (a) the interface of the welded zone, (b, c) SEM/BSE images of precipitates in the fusion zone, (c) BSE image of precipitates in the fusion zone, (d, e) SEM/BSE images of the interface of fusion zone, (f) magnified view of precipitates within the fusion zone.

Figure 4. Evidently, island-shaped and needle-like precipitates are randomly distributed outside the fusion zone (Figure 4(a)). In contrast, the tiny particles in the fusion zone are neatly arranged on the edge of the dendrites, and the space between the dendrites is about 2 ~ 5 μm (Figure 4(c)), demonstrating that the grains in the fusion zone are mainly composed of dendrites. The SEM image in Figure 5(f) further confirms the sizes of these particles being below 1 μm. It is important

to note that the uniform distribution of micron/sub-micron sized granular precipitates will effectively facilitate strength improvement of the alloy, suggesting that the strategies to obtain high-quality laser welded joint lies in reducing the width of the heat-affected zone.

To further analyze the elemental composition of precipitates within the fusion zone, the EDS method is employed, and the results are shown in Figure 6. Although EDS is not a fully quantitative chemical microanalysis analytical tool, rather a semiquantitative tool, but together with XRD, metallographic methods or good references, it is possible to infer reliable chemical composition data. Clearly, needle-like precipitates in the fusion zone are mainly composed of Al and Ce elements, and the atomic ratio is approximately 3:1. Combining this result with the XRD spectrums of the base metal, as depicted in Figure 3(c), it is evident that the needle-like precipitates within the fusion zone are $Al_{11}Ce_3$. Furthermore, EDS analysis of the tiny particles within the fusion zone indicates that they are mainly composed of Mg and Al elements, and the corresponding atomic ratio is approximately 3:2, which is inferred as $Mg_{17}Al_{12}$ Interestingly, rod-like precipitates are also observed in the fusion zone. However, the content is extremely low. EDS dotting found the rod-like precipitate consisting of Al, Mn, and Ce elements, and the atomic ratio is close to 10:2:7. According to the XRD results of the base metal, the rod-like precipitate is determined as the $Al_{10}Ce_2Mn_7$. At this point, the phase composition of precipitates within the fusion zone is well understood.

In fact, the morphology of precipitates in the fusion zone is closely related to the melting points and formation mechanisms of these precipitates. It is well known that the eutectic point of $Mg_{17}Al_{12}$ being 473 °C[18]. Evidently, as the fusion zone is heated up by the laser beam, the $Mg_{17}Al_{12}$ in the fusion zone melts and solutes into the Mg matrix under the stirring effect of the laser beam[19]. During the solidification of the fusion zone, Al atoms soluted in the melt eutectic and precipitate as the liquid-solid interface proceeds and the concentration of Al solutes in the residual melt eventually reaches the eutectic composition, thus facilitating the distribution of $Mg_{17}Al_{12}$ at the edge of dendrites[20]. Considering the high cooling rate of laser welding, these precipitated tiny $Mg_{17}Al_{12}$ particles do not have enough time to grow, thereby forming the typical micron/sub-micron-sized $Mg_{17}Al_{12}$ particles[20]. In comparison, rare-earth-containing intermetallics commonly possess high melting points, particularly for precipitates consisting of Al and rare-earth elements[21]. Research by Czerwinski[22] has shown that the melting point of $Al_{11}Ce_3$ is 1235 °C[22] and that of Al_4Ce, Al_2Ce, and Al_3Ce are 1251 °C[23], 1480 °C[23], and 1405 °C[23], respectively. Clearly, these rare-earth precipitates in the fusion zone partly melted and refined under the stirring effect of the laser beam. However, trace $Al_{11}Ce_3$ and $Al_{10}Ce_2Mn_7$ remain in the fusion zone, as displayed in Figures 5-6. EDS mapping results in Figure 7 provide additional evidence proving that sporadic $Al_{11}Ce_3$ and $Al_{10}Ce_2Mn_7$ remain in the fusion zone, demonstrating their excellent thermal stability, which is good for improving the heat resistance of Mg alloys.

3.3. Evolution mechanisms of precipitates within the fusion zone

To further interpret the evolution mechanisms of tiny particles during welding thermal cycles, particularly precisely evaluate the fraction of rare-earth particles within the fusion zone, solution treatment was employed, and the results are shown in Figures 8-9. The temperature applied was meticulously designed according to the Mg-Al and Al-Ce binary phase diagrams, which promotes the solution of $Mg_{17}Al_{12}$ into the Mg matrix, while the Ce-containing precipitates remain in the fusion zone. The comparison of precipitates in the fusion zone before and after the solution treatment is depicted in Figure 8.

Evidently, tiny particles before solution treatment are micron/sub-micron sized and neatly arranged at the edge of the dendrites, as shown in Figure 8(a). However, when

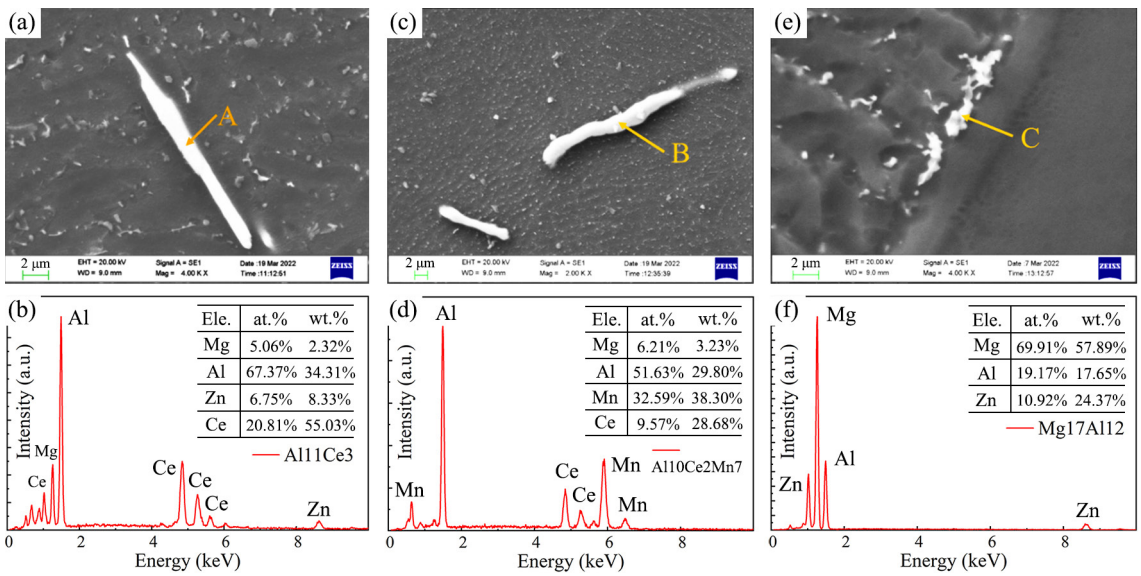

Figure 6. Morphology and EDS analysis of precipitated phases (a, b) $Al_{11}Ce_3$ phase (c, d) $Al_{10}Ce_2Mn_7$ phase (e, f) $Mg_{17}Al_{12}$ phase.

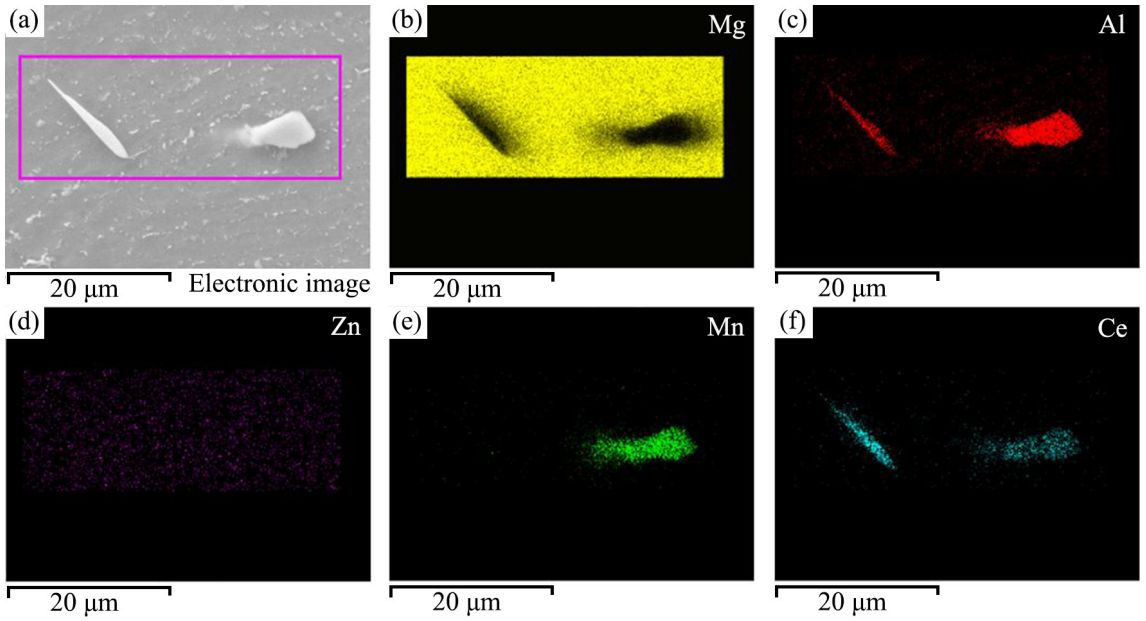

Figure 7. Morphology and EDS analysis of residual rare-earth precipitates. (a) SEM image of the fusion zone, (b~f) distribution of Mg/Al/Zn/Mn/Ce elements.

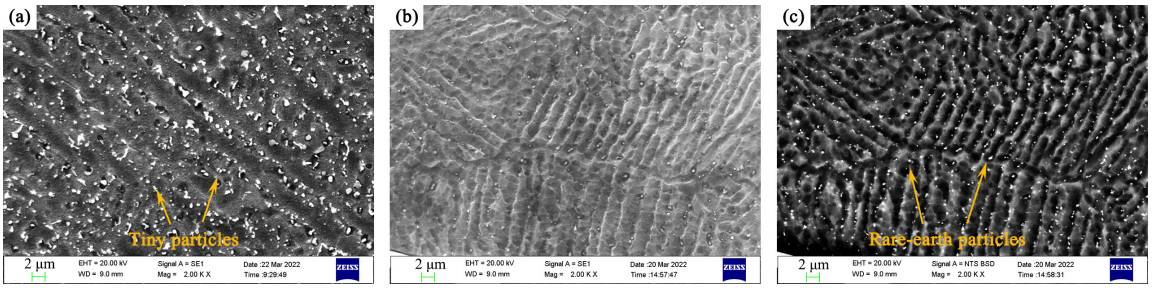

Figure 8. Precipitates within the fusion zone before and after solution treatment. (a) SEM image of precipitates within the fusion zone before solution treatment, (b) SEM image of precipitates after solution treatment, (c) BSE image of the precipitates after solution treatment.

these particles are kept at 420 °C for 20 hours, precipitates consisting of Mg and Al elements, primarily $Mg_{17}Al_{12}$, solute completely into the Mg matrix. In comparison, thermal stabled Ce-containing precipitates, including $Al_{11}Ce_3$ and $Al_{10}Ce_2Mn_7$, are remined in the fusion zone.

It is clear that the quantity of precipitates in the fusion zone decreases dramatically after the solution treatment. Interestingly, by observing the BSE image in Figure 8(c), it is evident that the size of rare-earth particles in the fusion zone is much smaller than that of the $Mg_{17}Al_{12}$ particles, with a diameter lower than 1 μm. Additionally, rare-earth particles account for a relatively small fraction of the total precipitates in the fusion zone. EDS mapping results in Figures 9-10 highly support the above deduction, reflecting the phase composition of precipitates within the fusion zone before and after the solution treatment. At this point, the morphology, phase composition, and distribution rules of conventional precipitates and rare-earth precipitates within the fusion zone are clear and well understood.

3.4. Mechanical properties of the laser welded joint

As the magnesium alloy sheets are lap welded, the tensile-shear test is carried out to evaluate the mechanical properties of the joint. The schematic diagram of the tensile-shear test and the corresponding results are shown in Figure 11. It is worth noting that during tensile-shear of the lap welded joint made from thin metal sheets, the joint rotates gradually with increasing tensile load. Eventually, the center of the two sheets aligned with the tensile direction before the sample fractured, indicating that the tensile shear of the welded joint equals the tensile of a single sheet. Interestingly, the heat-affected zone, namely the narrow region between the fusion zone and the base metal, becomes the weakest part and final load-bearing face. The load-bearing face during tensile-shear of the lap welded joint is detailed in Figure 11(c).

Evidently, results in Figure 11(a) indicate that the maximal tensile force of a 5.02 mm wide lap welded joint reaches 465 N, and the displacement reaches 0.51 mm. Take into consideration the gauge length being 5 mm and the thickness

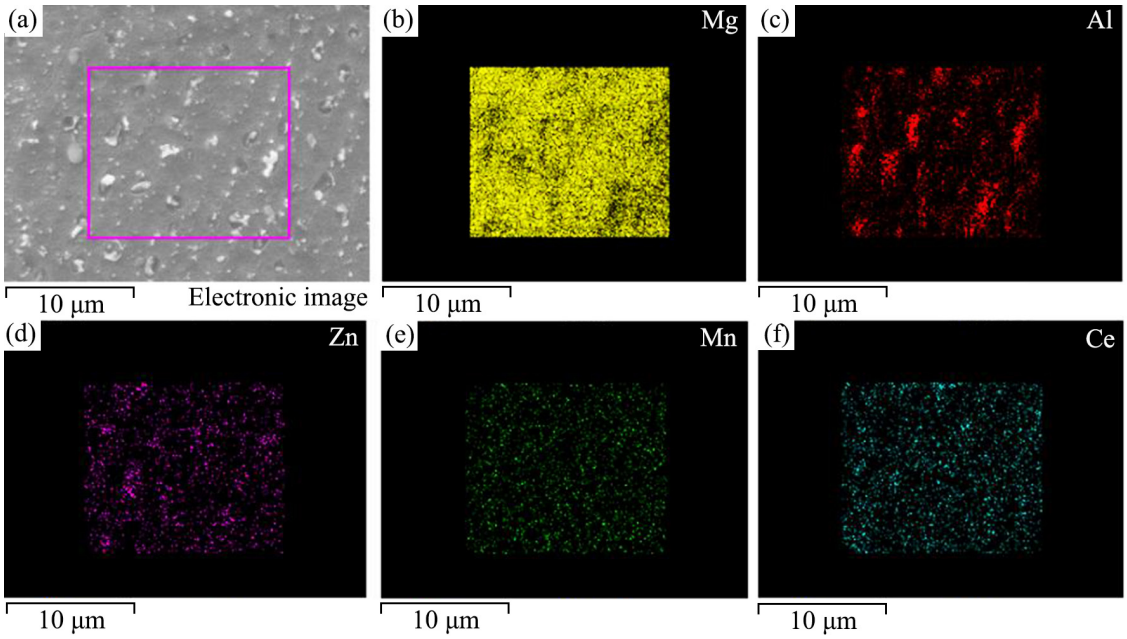

Figure 9. Precipitates in the fusion zone before solid solution treatment. (a) SEM image of the fusion zone, (b~f) distribution of Mg/Al/Zn/Mn/Ce elements.

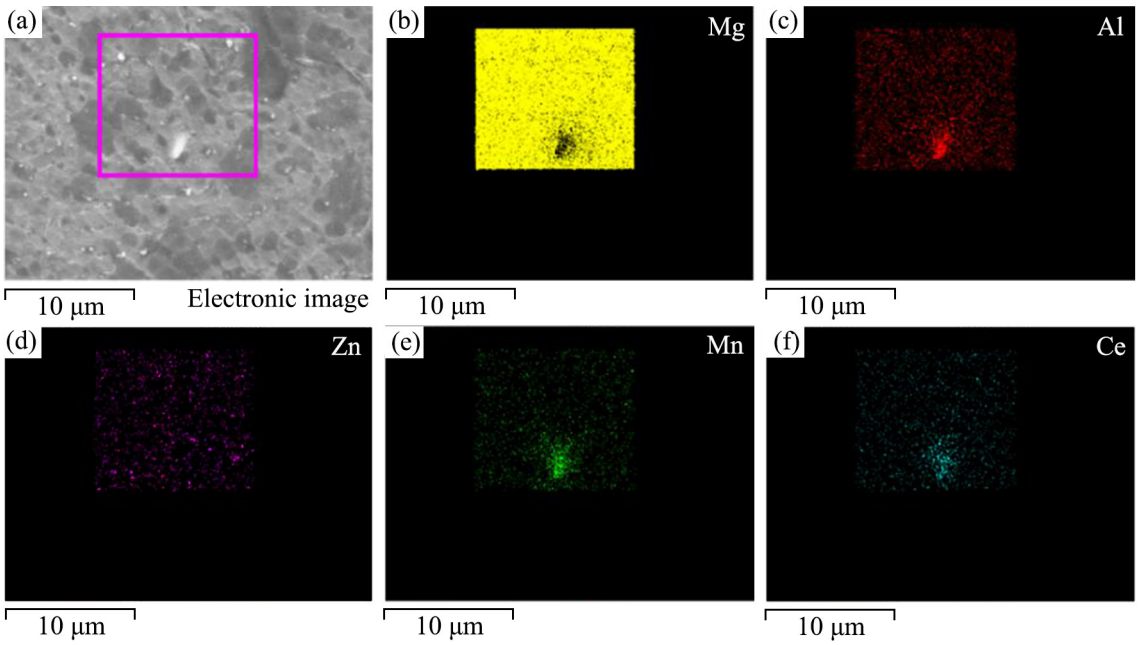

Figure 10. Precipitates in the fusion zone after solution treatment. (a) SEM image of the fusion zone, (b~f) distribution of Mg/Al/Zn/Mn/Ce elements.

of the sheet being 0.69 mm, where the sample fractured. Therefore, it is determined that the ultimate tensile strength of the welded joint is 134 MPa, and the corresponding elongation is 10.2%. This result is close to that of the base metal, which is 175 MPa and 13%, respectively, indicating that the tensile strength of the laser welded joint in this work reaches 76.6% that of the base metal, demonstrating the good welding quality of magnesium alloy through laser welding in this work.

The fracture of the welded joint is shown in Figure 12. As the fusion zone is enhanced by the micron/sub-micron-sized particles, the sample fractured at positions between the

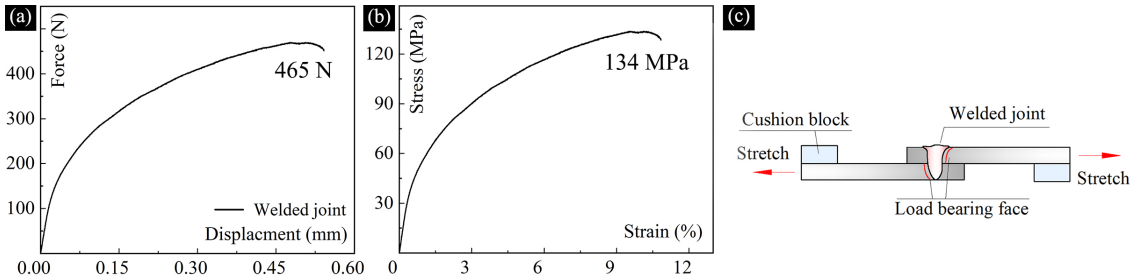

Figure 11. Tensile-shear test of the laser welded joint. (a) load-displacement curve, (b) strain-stress curve, (c) schematic diagram of the tensile-shear test.

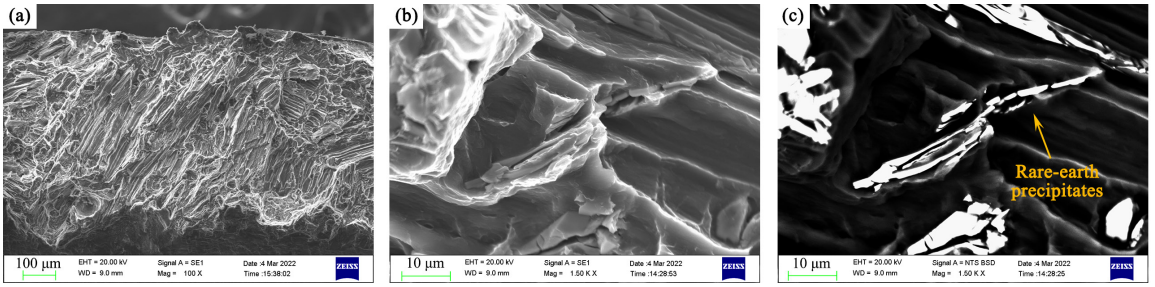

Figure 12. Fracture of the welded joint. (a) fracture, (b~c) SEM/BSE image of precipitates on the surface of the fracture.

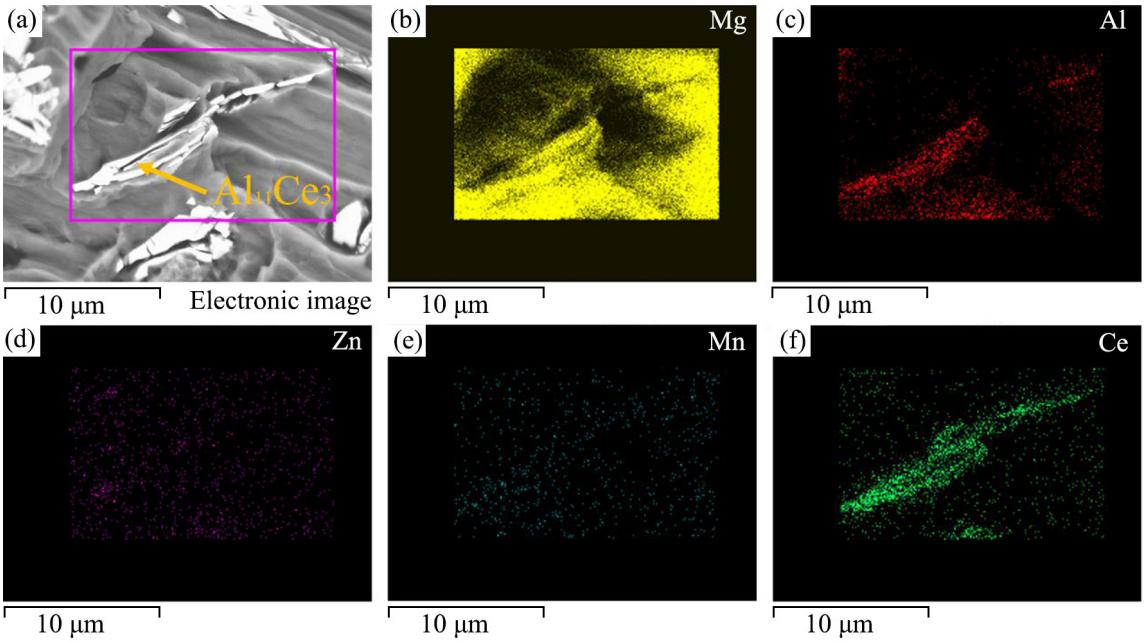

Figure 13. EDS mapping of precipitates on the surface of the fracture. (a) morphology of the fracture, (b~f) distribution of Mg/Al/Zn/Mn/Ce elements.

fusion zone and the base metal, i.e. the heat-affected zone. Evidently, the SEM image in Figure 12(a) indicates that the fracture mode is a cleavage fracture, and the magnified view of the fracture found several needle-like precipitates on the surface of the fracture. Moreover, the needle-like precipitates break into pieces. EDS mapping analysis was employed to further identify the phase composition of these precipitates, and the results are shown in Figure 13. Clearly, these precipitates are mainly composed of Al and Ce elements. Combining the morphology of these precipitates, they are inferred as $Al_{11}Ce_3$.

It is worth noting that $Al_{11}Ce_3$ is incoherent with the Mg matrix. During the tensile of the welded joint, stress at the phase boundaries increases dramatically, particularly for incoherent boundaries. As a result, the needle-like precipitates break into pieces during the process of resisting matrix deformation, typical morphology of the broken precipitates is depicted in Figure 12(c). More importantly, stress concentration at the incoherent phase boundaries of sharp-shaped needle-like $Al_{11}Ce_3$ facilitates the cracking of this boundary, eventually leading to the failure of the welded joint. Therefore, it is recommended to break the coarse, sharp-shaped precipitates originally in the alloy, and promote the formation of granular precipitates within the welded joints, these strategies play significant roles in improving the mechanical properties of the laser welded joints.

4. Conclusion

In this paper, a fiber laser is utilized to weld Ce-containing Mg alloys. The microstructure of the fusion zone and the HAZ is emphatically analyzed, revealing that typical micron/sub-micron-sized particles are neatly distributed within the fusion zone. The focus is placed on the formation and distribution rules of these precipitates within the fusion zone, particularly the evolution mechanisms of these precipitates during thermal cycles, thus deducing the influence of rare-earth particles on the mechanical properties of the welded joints. The conclusions of this work are listed as follows:

(1) 0.7 mm thick Ce-containing Mg alloys are successfully welded through fiber laser welding. The observations indicate that the width of the fusion zone on the top surface of the welded joint is 1087 μm, while that on the contact interface of the two sheets is 810 μm, both are wider than the thickness of a single sheet.

(2) Microstructural observations reveal that micron/sub-micron-sized particles are formed within the fusion zone. These tiny particles are neatly arranged at the edge of the dendrites. The precipitation rules of these tiny particles are closely related to their eutectic points and formation mechanisms.

(3) Solution treatment of the fusion zone suggests that the tiny particles within the fusion are composed of not only conventional precipitates like $Mg_{17}Al_{12}$ but also a small fraction of rare-earth precipitates like $Al_{11}Ce_3$ and $Al_{10}Ce_2Mn_7$.

(4) Mechanical property test results indicate the welded joint fractures within the HAZ. The ultimate tensile strength of the welded joint during the tensile-shear test is 134 MPa, accounting for 76.6% that of the base metal, suggesting a good welding quality of the Ce-containing Mg alloy.

(5) Based on the above results, a feasible solution for improving the welding quality of rare-earth Mg alloy is proposed, namely promoting the refinement of precipitates originally in the alloy and forming tiny particles consisting of both conventional and rare-earth particles within the fusion zone.

5. References

1. Ren L, Fan L, Zhou M, Guo Y, Zhang Y, Boehlert CJ, et al. Magnesium application in railway rolling stocks: a new challenge and opportunity for lightweighting. Int J Lightweight Mater Manuf. 2018;1(2):81-8.
2. Jayasathyakawin S, Ravichandran M, Baskar N, Anand Chairman C, Balasundaram R. Mechanical properties and applications of Magnesium alloy–Review. Mater Today Proc. 2020;27:909-13.
3. Zhu J, Cheng X, Zhang L, Hui X, Wu Y, Zheng H, et al. Microstructures, wear resistance and corrosion resistance of CoCrFeNi high entropy alloys coating on AZ91 Mg alloy prepared by cold spray. J Alloys Compd. 2022;925:166698.
4. Deng J, Tian J, Zhou Y, Chang Y, Liang W, Ma J. Plastic deformation and fracture mechanisms of rolled Mg-8Gd-4Y-Zn and AZ31 magnesium alloys. Mater Des. 2022;223:111179.
5. Zhang H, Guo B, Du W, Cong X, Chen C. Study on the weld formation, microstructure and mechanical properties of AZ31B Mg alloy in AC/DC mixed gas tungsten arc welding process. J Mater Res Technol. 2022;18:3664-72.
6. Cao X, Jahazi M, Immarigeon JP, Wallace W. A review of laser welding techniques for magnesium alloys. J Mater Process Technol. 2006;171(2):188-204.
7. Song J, She J, Chen D, Pan F. Latest research advances on magnesium and magnesium alloys worldwide. J Magnes Alloys. 2020;8(1):1-41.
8. Wu G, Wang C, Sun M, Ding W. Recent developments and applications on high-performance cast magnesium rare-earth alloys. J Magnes Alloys. 2021;9(1):1-20.
9. Silva EPD, Marques F, Nossa TDS, Alfaro U, Pinto HC. Impact of Ce-base mischmetal on the microstructure and mechanical behavior of ZK60 magnesium casting alloys. Mater Sci Eng A. 2018;723:306-13.
10. Tong G, Liu H, Liu Y. Effect of rare earth additions on microstructure and mechanical properties of AZ91 magnesium alloys. Trans Nonferrous Met Soc China. 2010;20:s336-40.
11. Fu Q, Li Y, Liu G, Li H. Low cycle fatigue behavior of AZ91D magnesium alloy containing rare-earth Ce element. Procedia Eng. 2012;27:1794-800.
12. Niu J, Chen Q, Xu N, Wei Z. Effect of combinative addition of strontium and rare earth elements on corrosion resistance of AZ91D magnesium alloy. Trans Nonferrous Met Soc China. 2008;18(5):1058-64.
13. Li Q, Xiong W, Yu M, Li J, Liu L, Zhu G, et al. Effect of Ce content on performance of AZ31 magnesium alloy anode in air battery. J Alloys Compd. 2022;891:161914.
14. Li Z, Wang J, Yan R, Chen Z-Y, Ni T-Y, Dong Z-Q, et al. Effect of Ce addition on hot deformation behavior and microstructure evolution of AZ80 magnesium alloy. J Mater Res Technol. 2022;16:1339-52.
15. Juan S, Feng G, Huisheng C, Liang L. Structural analysis of Al–Ce compound phase in AZ-Ce cast magnesium alloy. J Mater Res Technol. 2019;8(6):6301-7.
16. Al-Kazzaz H, Medraj M, Cao X, Jahazi M. Nd: YAG laser welding of aerospace grade ZE41A magnesium alloy: Modeling and experimental investigations. Mater Chem Phys. 2008;109(1):61-76.
17. Wang Z, Gao M, Tang H, Zeng X. Characterization of AZ31B wrought magnesium alloy joints welded by high power fiber laser. Mater Charact. 2011;62(10):943-51.
18. Guldberg S, Ryum N. Microstructure and crystallographic orientation relationship in directionally solidified Mg–Mg17Al12-eutectic. Mater Sci Eng A. 2000;289(1-2):143-50.
19. Padmanaban G, Balasubramanian V. Effects of laser beam welding parameters on mechanical properties and microstructure of AZ31B magnesium alloy. Trans Nonferrous Met Soc China. 2011;21(9):1917-24.
20. Al Bacha S, Desmedt A, Zakhour M, Nakhl M, Bobet J-L. Mechanism of hydrogen formation during the corrosion of Mg17Al12. Electrochem Commun. 2020;119:106813.
21. Luo Q, Guo Y, Liu B, Feng Y, Zhang J, Li Q, et al. Thermodynamics and kinetics of phase transformation in rare earth–magnesium alloys: a critical review. J Mater Sci Technol. 2020;44:171-90.

22. Czerwinski F. Thermal stability of aluminum–cerium binary alloys containing the Al–Al11Ce3 eutectic. Mater Sci Eng A. 2021;809:140973.

23. Chen Y, Zhu Z, Zhou J. Study on the strengthening mechanism of rare earth yttrium on magnesium alloys. Mater Sci Eng A. 2022;850:143513.